S & M 4203

Damage Diagnosis for Wet Joints of Prefabricated Beam Bridges Monitored within One Cluster Using the Data Obtained from Distributed Optical Sensing Fibers

Binju Zhang, 1 Chen Li, 2 Litao Yu, 1 Chen Hua, 1 Yifan Lu, 1 and Yang Liu^{2*}

¹Tongxiang Sutai Expressway Investment and Development Co., Ltd, Tongxiang 310000, China ²School of Transportation Science and Engineering, Harbin Institute of Technology, Harbin 150090, China

(Received June 5, 2025; accepted October 3, 2025)

Keywords: prefabricated beam bridge monitored within one cluster, damage diagnosis of beam bridge wet joints, curvature, distributed optical sensing fiber

The cracking and spalling of wet joint concrete are common forms of wet joint damage in prefabricated beam bridge structures; however, existing diagnosis methods are often insensitive to damage and are overly susceptible to environmental effects and random vehicle loads. To address this, we propose a diagnostic method for wet joint damage in such clusters on the basis of data obtained from distributed optical sensing fibers. Distributed optical sensing fibers are deployed along the top and bottom of the main girder webs, and a Brillouin optical time domain analysis (BOTDA) analyzer is used to collect strain at the corresponding locations, from which the sectional curvature is computed. By exploiting the cluster's spatiotemporal correlation, a bidirectional long short-term memory (Bi-LSTM) network is constructed to predict the sectional curvature of bridges with identical configurations within the cluster. On this basis, a cluster-level wet joint damage diagnosis index is formulated, and a cross-validation strategy is employed to identify wet joint damage across the cluster. Under random vehicle loads, a numerical case study of wet joint damage in a prefabricated beam bridge cluster is conducted to compare the proposed approach with conventional methods, thereby verifying its effectiveness. In addition, monitoring data from three adjacent bridges in an actual cluster are used for further validation. The results indicate that the proposed method satisfies the requirements for cluster-level wet joint damage diagnosis and can be applied to the real-time monitoring and assessment of prefabricated beam bridge clusters.

1. Introduction

According to the 2024 Industry Development Bulletin released by the Ministry of Transport of China, (1) as of the end of 2023, there were approximately 1.0793 million highway bridges in China, among which 890000 were small- and medium-span bridges, making them the dominant structural form in highway bridge construction. Prefabricated beam bridges have become a common type for small- and medium-span bridges due to their short construction periods and

*Corresponding author: e-mail: <u>ly7628@hit.edu.cn</u> <u>https://doi.org/10.18494/SAM5771</u>

ease of quality control.⁽²⁾ For prefabricated beam bridges, a reliable transverse connection system is essential to ensure integrated structural performance. However, during actual operation, increased traffic loads, environmental erosion, and other external factors often lead to longitudinal cracking, water seepage, and beam misalignment in transverse connection areas. These issues result in uneven load distributions among the beams, causing single-beam load-bearing conditions,^(3,4) which severely impact the load-bearing capacity of the superstructure in prefabricated beam bridges.

To investigate the damage patterns of transverse connection systems in prefabricated beam bridges, Xia *et al.*⁽⁵⁾ derived the relationships between joint conditions and transverse load distribution coefficients, transforming the quantitative analysis of transverse cooperative performance into the identification of transverse load distribution influence lines. Yang *et al.*⁽⁶⁾ established a spring-jointed plate model based on the traditional articulated plate method and analyzed the relationship between shear forces and transverse connection system damage. Li *et al.*⁽⁷⁾ proposed a new method using model updating and an orthogonal matching pursuit algorithm to accurately identify the degree and location of joint damage on the basis of the vertical displacement of a single measurement point. By solving the characteristic equation of a multiple-girder system, Shang *et al.*⁽⁸⁾ proposed a method of determining baseline joint stiffness via design data and finite element models, and developed a comprehensive evaluation framework for joints. Han *et al.*⁽⁹⁾ introduced a monitoring and evaluation method for transverse connection stiffness, which is based on multiple-girder theory and enables the diagnosis and localization of joint damage.

With the continuous advancement of bridge health monitoring technology, the number of studies on the diagnosis of transverse connection system damage through structural response monitoring has increased. Dan et al. (10) validated the strain correlation coefficient index via real bridge monitoring data and proposed a joint damage monitoring index on the basis of displacement spectrum similarity. Hu et al. (11) utilized computer vision technology to measure structural displacement and assess joint damage conditions using relative displacement as a diagnostic indicator. However, the sensitivity of the proposed indicator varies with the degree of damage. Gong et al. (12) employed the recursive least squares method to evaluate joint stiffness in real time and studied the effects of joint damage on the bridge frequency, damping ratio, and modal shape. Zhan et al. (13) diagnosed joint damage by calculating vehicle-bridge interaction responses and updating the finite element model (FEM) on the basis of monitoring data. Abedin et al. (14) updated FEM through static and dynamic load tests, and established a damage index for joint damage assessment. Han et al. (15) proposed the transverse modal shape damage index to locate and assess the degree of joint damage. Reiff et al. (16) utilized strain monitoring data to construct a live load distribution factor for bridge damage assessment. The aforementioned studies achieved real-time diagnoses of transverse connection system damage to some extent through FEM updating(13,14,17) and operational monitoring.(10,11,15,16) However, these methods have several limitations, such as the requirement for onsite testing^(5,13,14) and stable traffic loads, (10) which lead to insufficient sensitivity in actual applications and fail to meet the demands of long-term bridge monitoring. In this context, distributed optical fiber sensing technology presents an effective solution to these challenges. It enables the collection of high-density strain

response and structural temperature field data, making it suitable for structural damage diagnosis. (17–22) Currently, distributed optical fiber monitoring technology has been widely applied in various fields, including tunnel settlement, (21) bridge deformation, (22) and landslide monitoring. (23)

To effectively monitor wet joint damage in bridges with identical structural configurations within a cluster of prefabricated beam bridges, we propose a diagnostic method for wet joint damage in such a cluster on the basis of data obtained from distributed optical sensing fibers. Distributed optical sensing fibers are deployed along the top and bottom of the main girder webs, and a BOTDA analyzer is used to collect strain at the corresponding locations, from which the sectional curvature of the girders is computed. Drawing on the structural and loading similarity of the cluster, we derive the spatiotemporal correlation of the sectional curvature among bridges; on this basis, we construct a Bi-LSTM network to predict the sectional curvature of bridges with identical configurations, formulate a cluster-level wet joint damage diagnosis index, and employ a cross-validation strategy to identify wet joint damage across the cluster. Under random vehicle loads, a numerical case study of wet joint damage in a prefabricated beam bridge cluster is conducted to compare the proposed method with conventional approaches, thereby verifying its effectiveness. In addition, monitoring data from three adjacent bridges in an actual cluster are used for further validation. The results indicate that the proposed method satisfies the requirements for cluster-level wet joint damage diagnosis and can be applied to the real-time monitoring and assessment of prefabricated beam bridge clusters. Compared with commonly used wet joint damage diagnosis methods for prefabricated beam bridges, our approach avoids reliance on a single-bridge absolute baseline or bridge-by-bridge model updating. Instead, it employs relative comparisons among bridges of identical configurations within a cluster together with a cross-validation strategy to offset environmental and loading disturbances, thereby improving the detectability of slight wet-joint damage and enhancing practical applicability.

The contents of this study are organized as follows. In Sect. 2, we elaborate on the proposed method in detail. In Sect. 3, we validate the effectiveness of the proposed method using numerical examples and real-world measured data. In Sect. 4, we summarize the conclusions of this study.

2. Algorithm Theory

2.1 Curvature calculation using the strain measured by the distributed optical sensing fiber

Prefabricated beam bridges monitored within one cluster refer to a group of medium- and small-span bridges within urban elevated roads or highway routes, as illustrated in Fig. 1. Owing to their location on the same traffic route, these bridges are subjected to highly similar external loads, such as comparable overall temperature and vehicle loads. Furthermore, since prefabricated beam bridges monitored within one cluster are typically constructed simultaneously, the degrees of shrinkage and creep in the structural materials of each bridge are



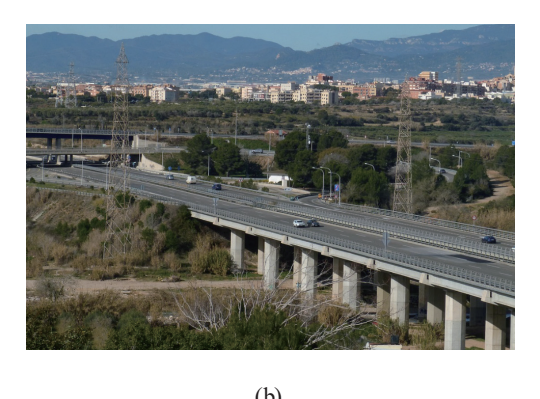


Fig. 1. (Color online) Clusters of prefabricated beam bridges. (a) Urban elevated viaduct cluster and (b) cluster of highway girder bridges.

also similar. These similarities in structure and loading conditions result in a high degree of correlation in the monitoring data across the bridges monitored within one cluster.

Distributed optical fiber sensing technology employs distributed optical sensing fibers as sensing elements to detect the deformation and temperature changes of a bridge, correlating these measurements with the positions along the distributed optical sensing fiber, thereby enabling long-distance distributed monitoring. As illustrated in Fig. 2, when the bridge structure deforms, it induces a change in Brillouin center frequency at the corresponding position of the optical fiber, resulting in a Brillouin frequency shift. By leveraging the relationship between the Brillouin frequency shift and strain, strain monitoring data for the bridge structure can be obtained. Assuming that the temperature remains constant during the strain acquisition process, the strain response can be expressed as

$$\varepsilon = \varepsilon_0 + \Delta \varepsilon = \varepsilon_0 + \frac{v_B - v_0}{C_{\varepsilon}},\tag{1}$$

where ε represents the measured strain, ε_0 the initial strain, v_B the measured central spectral frequency, v_0 the initial central spectral frequency, and C_{ε} the strain influence coefficient.

For this purpose, a distributed optical sensing fiber monitoring loop is installed at both the top and bottom of the web of the main beam of the prefabricated beam bridge. In this setup, strain monitoring data are collected at different heights of the main beam of the bridge, and the sectional curvature of the main beam is subsequently calculated using Eq. (2). The layout of the monitoring loop is illustrated in Fig. 2.

$$\kappa_i = \frac{\varepsilon_i^b - \varepsilon_i^t}{h_i^b + h_i^t} = \frac{\varepsilon_i^b - \varepsilon_i^t}{h_i}, \quad i = 1, 2, \dots, n$$
 (2)

Here, κ_i represents the average curvature of the i-th cross section; ε_i^t and ε_i^b the strain values at the top and bottom measurement points of the i-th cross section of the main beam of the bridge,

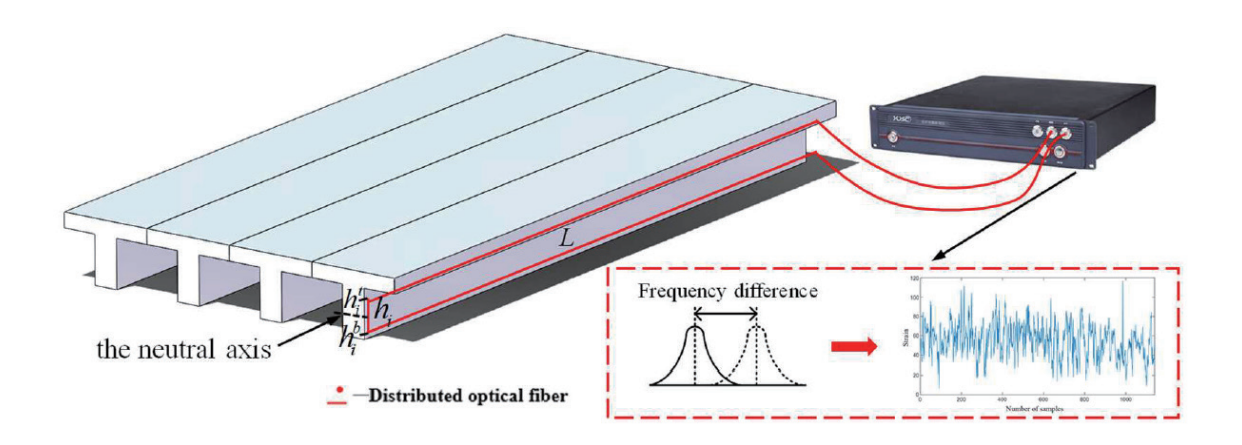


Fig. 2. (Color online) Schematic of the principle of distributed optical fiber monitoring technology.

and h_i^t and h_i^b the distances from the top and bottom measurement points of the *i*-th cross section of the main beam of the bridge to the neutral axis, respectively.

2.2 Bi-LSTM-based wet joint damage diagnosis of prefabricated beam bridges monitored within one cluster

$$\boldsymbol{\kappa}_{r}^{j} = \left\{ \kappa_{r,1}^{j}, \kappa_{r,2}^{j}, \cdots, \kappa_{r,i}^{j}, \cdots, \kappa_{r,N}^{j} \right\}^{T}, \quad i = 1, 2, \cdots, N$$
(3)

$$\boldsymbol{\kappa}^{j} = \left[\boldsymbol{\kappa}_{1}^{j}, \boldsymbol{\kappa}_{2}^{j}, \dots, \boldsymbol{\kappa}_{r}^{j}, \dots, \boldsymbol{\kappa}_{T}^{j}\right], \quad r = 1, 2, \dots, T$$

$$(4)$$

$$\boldsymbol{\kappa} = \left[\boldsymbol{\kappa}^{1}, \boldsymbol{\kappa}^{2}, \dots, \boldsymbol{\kappa}^{j}, \dots, \boldsymbol{\kappa}^{W}\right], \quad j = 1, 2, \dots, W$$
(5)

$$\overline{\mathbf{\kappa}} = Savitzky - Golay(\mathbf{\kappa}) \tag{6}$$

In Eqs. (2) to (6), $\kappa_{r,i}^J$ represents the curvature measurement at the *i*-th sensor of the *j*-th bridge at time step r, κ_r^j the curvature vector of the *j*-th bridge at time step r, κ^j the curvature matrix of the *j*-th bridge, κ the combined curvature matrix of prefabricated beam bridges monitored within one cluster, $Savitzky-Golay(\cdot)$ the Savitzky-Golay filter operator, and $\overline{\kappa}$ the denoised curvature matrix of prefabricated beam bridges monitored within one cluster, obtained by applying S-G to κ .

Under load, when the wet joints are intact, the superstructure exhibits good transverse force transmission, and the curvatures of each beam demonstrate a relatively stable strong correlation. However, when the wet joints are damaged, as the damage severity increases, the force transmission between adjacent beams at the damaged wet joint locations significantly deteriorates. Consequently, the correlation among the curvatures of each beam gradually weakens, deviating from the original stable trend. The deformation behavior of the superstructure

before and after damage is illustrated in Fig. 3. On the basis of this characteristic, the curvature vector angle between adjacent beams at the same moment is calculated using Eq. (7), and the angle vector is constructed using Eq. (8).

$$\theta_r^j = subspace\left(\overline{\kappa}_r^j, \overline{\kappa}_r^{j+1}\right) \tag{7}$$

$$\boldsymbol{\theta}_{D}^{j} = \left\{ \theta_{1}^{j}, \theta_{2}^{j}, \dots, \theta_{r}^{j}, \dots, \theta_{T}^{j} \right\}$$
(8)

Here, θ_r^j represents the angle between the *j*-th curvature vectors at time *r* in prefabricated beam bridges monitored within one cluster, $subspace(\cdot)$ the vector-angle computation function, and $\boldsymbol{\theta}_D^j$ the angle between the *j*-th curvature vectors of prefabricated beam bridges monitored within one cluster.

In accordance with the distribution of measurement points on beam bridges monitored within one cluster, the main beam of the bridges is discretized. Consequently, the dynamic equilibrium equation of the structure can be formulated as

$$\boldsymbol{M}(x,t)\ddot{\boldsymbol{\omega}}_{r}^{j} + \boldsymbol{C}(x,t)\dot{\boldsymbol{\omega}}_{r}^{j} + \boldsymbol{K}(x,t)\boldsymbol{\omega}_{r}^{j} = \boldsymbol{F}^{r}(x,t), \tag{9}$$

where, M(x,t) represents the mass matrix of the prefabricated beam bridges, C(x,t) the damping matrix of the prefabricated beam bridges, K(x,t) the stiffness matrix of the prefabricated beam bridges, $F^r(x,t)$ the external load vector at time step r, $\dot{\boldsymbol{\omega}}_r^j$ the velocity vector of the j-th main beam at time step r, and $\ddot{\boldsymbol{\omega}}_r^j$ the acceleration vector of the j-th main beam at time step r.

By applying the Laplace transform to both sides of Eq. (9), we can derive the following result:

$$\mathbf{Z}(x,t)\boldsymbol{\omega}_r^j = \mathbf{F}^r. \tag{10}$$

Here, Z(x,t) represents the displacement impedance matrix.

Since the beam bridges monitored within one cluster are situated on the same traffic route, they experience highly similar external loads. Consequently, for two bridges, p and v, monitored

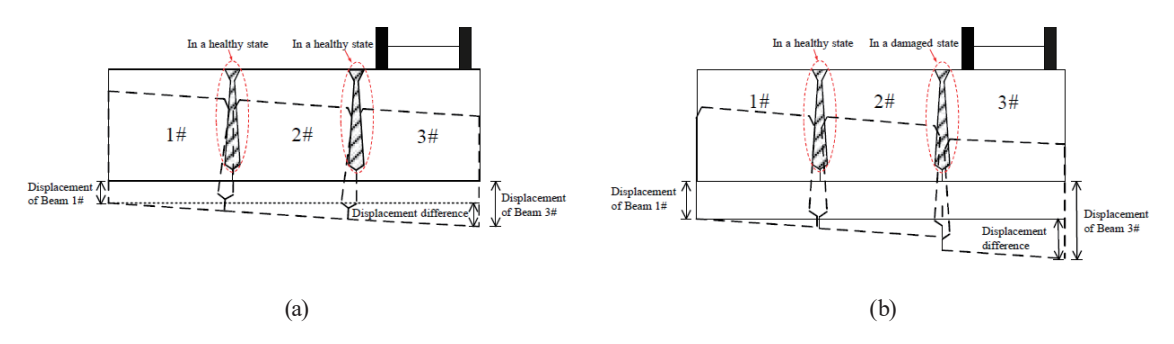


Fig. 3. (Color online) Schematic diagrams of superstructure deformation (a) before and (b) after wet joint damage.

within one cluster that shares identical structural designs, the following relationships can be established concerning their deformations:

$$\mathbf{Z}^{p}(x,t)\boldsymbol{\omega}_{r}^{p,j} = \mathbf{Z}^{v}(x,t)\boldsymbol{\omega}_{r}^{v,j},\tag{11}$$

$$\boldsymbol{\omega}_r^{p,j} = (\boldsymbol{Z}^p(x,t))^{-1} \boldsymbol{Z}^{\nu}(x,t) \boldsymbol{\omega}_r^{\nu,j}, \tag{12}$$

$$\boldsymbol{\omega}_{x}^{p,j} = \boldsymbol{\Psi}(x,t)\boldsymbol{\omega}_{x}^{v,j}. \tag{13}$$

Here, $\mathbf{Z}^p(x,t)$ represents the displacement impedance matrix of bridge p, $\mathbf{Z}^v(x,t)$ the displacement impedance matrix of bridge v, and $\mathbf{\Psi}(x,t)$ the deformation mapping matrix from bridge v to bridge p.

Furthermore, drawing on the principles of material mechanics, the relationship between the sectional curvature of the main beam and the vertical deflection can be formulated as

$$\kappa(x) = \frac{d^2\omega(x)}{dx^2}.$$
 (14)

By combining Eqs. (13) and (14), the sectional curvature of the main beam of prefabricated beam bridges p and v, which have identical structures within the cluster, can be formulated as

$$\boldsymbol{\kappa}_r^{p,j} = \boldsymbol{\Psi}(x,t)\boldsymbol{\kappa}_r^{v,j} + \boldsymbol{\Psi}'(x,t)\boldsymbol{\omega}_r^{v,j}. \tag{15}$$

In this equation, $\kappa_r^{p,j}$ represents the curvature vector of the *j*-th beam of bridge *p* at time step *r* and $\kappa_r^{v,j}$ the curvature vector of the *j*-th beam of bridge *v* at time step *r*.

For prefabricated beam bridges, given that the cross section of the main beam exhibits minimal variation along the longitudinal direction of the bridges, the change along the x-direction can be neglected. Under these conditions, Eq. (15) can therefore be simplified as

$$\boldsymbol{\kappa}_r^{p,j} = \boldsymbol{\Psi}(t) \boldsymbol{\kappa}_r^{v,j}. \tag{16}$$

Equation (16) clearly shows that a time-varying mapping relationship exists among the curvature vectors of identical prefabricated beam bridges monitored within one cluster. On this basis, a Bi-LSTM network is constructed by taking bridge p as the reference bridge and bridge v as the target bridge for diagnosis. The structure of the network is presented in Fig. 4.

To increase the stability of the Bi-LSTM network, the Z-score method is employed to preprocess the network input data. The z-score method standardizes data by subtracting the mean from each value and dividing by the standard deviation. The loss function of the Bi-LSTM network is quantified using the root mean square error (*RMSE*). The model parameters are updated through the minimization of the loss function, as presented in Eq. (17).

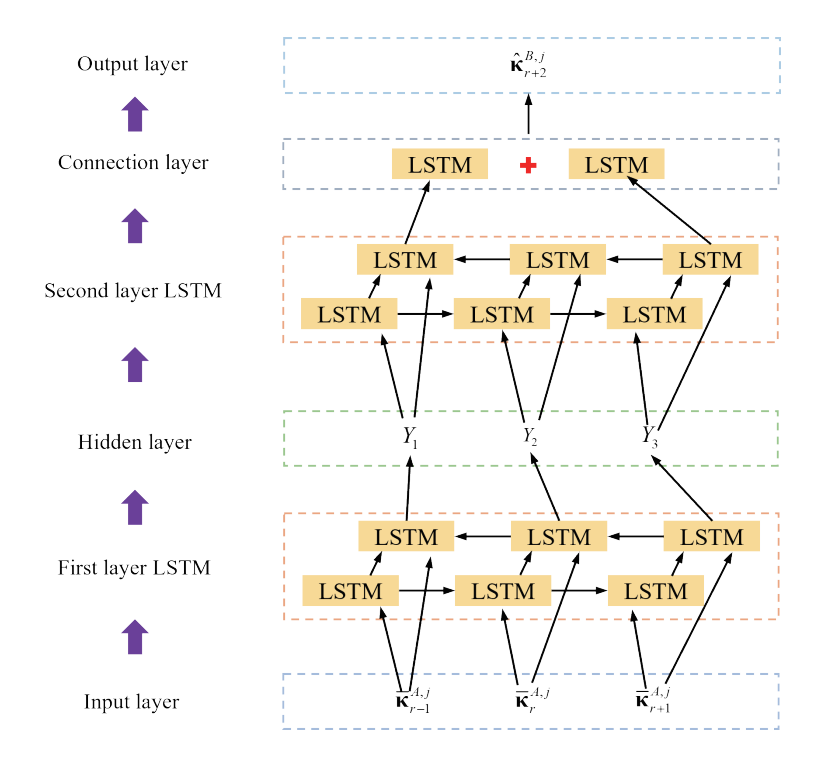


Fig. 4. (Color online) Schematic diagram of the Bi-LSTM network.

$$L(\Theta) = \min\left(\left\|\hat{\kappa}_r^{p,v,j} - \overline{\kappa}_r^{v,j}\right\|_2\right) \tag{17}$$

Here, $\hat{\kappa}_r^{p,v,j}$ represents the predicted value of $\overline{\kappa}_r^{v,j}$, Θ the model training parameters, min(·) the minimization operator, and $L(\cdot)$ the loss function.

On the basis of the constructed Bi-LSTM network, the residual vector between the calculated and predicted V-bridge curvature vectors is derived using Eqs. (7) and (8).

$$\boldsymbol{\xi}^{p,v,j} = \hat{\boldsymbol{\theta}}_{D}^{p,v,j} - \boldsymbol{\theta}_{D}^{v,j} = \left\{ \xi_{1}^{p,v,j}, \xi_{2}^{p,v,j}, \dots, \xi_{r}^{p,v,j}, \dots, \xi_{T}^{p,v,j} \right\}$$
(18)

In Eq. (18), $\xi_r^{p,v,j}$ represents the *j*-th residual value of bridge v at time step r, $\hat{\boldsymbol{\theta}}_D^{p,v,j}$ the predicted value of $\boldsymbol{\theta}_D^{v,j}$, and $\boldsymbol{\xi}^{p,v,j}$ the residual vector for the *j*-th girder of bridge v.

A wet joint damage diagnosis index is formulated on the basis of the residual vector obtained from Eq. (18).

$$\psi_r^{p,v,j} = \left[\frac{\left(\xi_r^{p,v,j} - \mu_j\right)^2}{S_j} \right]^{0.5}$$
(19)

In Eq. (19), μ_j represents the mean of the elements in $\xi_r^{p,v,j}$, S_j represents the covariance of the elements in $\xi_r^{p,v,j}$, and $\psi_r^{p,v,j}$ represents the wet joint damage diagnosis index of the *j*-th wet joint at the *r*-th moment of bridge *v*.

On the basis of the constructed wet joint damage diagnosis index, the wet joint damage threshold is determined as

$$\gamma_i^{p,v} = \alpha G_{0.95} (\psi_r^{p,v,j}),$$
(20)

where $\gamma_j^{p,\nu}$ represents the threshold for the *j*-th damage diagnosis index, $G_{0.95}(\cdot)$ the 95th-percentile (quantile) function at the 95% confidence level, and α the safety factor, which is recommended to be no less than 1.5.

To prevent the misjudgment of the condition of the wet joints in the main beams of prefabricated beam bridges monitored within one cluster, a cross-validation strategy is employed to assess the damage status of these wet joints. The procedure is as follows: First, one bridge is randomly selected from the cluster as the reference bridge, and the proposed algorithm is applied to determine whether damage to the wet joints between the reference bridge and any other bridge in the cluster occurs. The role of the reference bridge is then cyclically reassigned until all the bridges in the cluster have served as the reference bridge. Finally, a damage discrimination matrix is constructed on the basis of the diagnostic results of all the bridges in the cluster, enabling the final determination of the damage conditions of the wet joints in the main beams of the beam bridges within the cluster.

Assuming that there are N structurally identical bridges in prefabricated beam bridges monitored within one cluster, the damage discrimination matrix for the j-th wet joint in the cluster is expressed as

$$U_r^{p,v,j} = \begin{cases} \psi_r^{p,v,j} - \gamma_j^{p,v}, & (\psi_r^{p,v,j} > \gamma_j^{p,v}) \\ 0, & (\psi_r^{p,v,j} < \gamma_j^{p,v}) \end{cases}$$
(21)

$$U^{p,v,j} = \frac{\sum_{r=1}^{T} U_r^{p,v,j}}{T},$$
(22)

$$U^{j} = \begin{bmatrix} U^{2,1,j} & U^{3,1,j} & \cdots & U^{p,1,j} & \cdots & U^{N,1,j} \\ U^{1,2,j} & U^{3,2,j} & \cdots & U^{p,2,j} & \cdots & U^{N,2,j} \\ \vdots & \vdots & \ddots & \vdots & \ddots & \vdots \\ U^{1,v,j} & U^{2,v,j} & \cdots & U^{p,v,j} & \cdots & U^{N,v,j} \\ \vdots & \vdots & \ddots & \vdots & \ddots & \vdots \\ U^{1,N,j} & U^{2,N,j} & \cdots & U^{p,N,j} & \cdots & U^{N-1,N,j} \end{bmatrix}.$$
(23)

In Eqs. (21) to (23), $\psi_r^{p,v,j}$ denotes the wet joint damage diagnosis index for the *j*-th wet joint at the *r*-th moment, with *p* serving as the reference bridge and *v* being the bridge under diagnosis; $U_r^{p,v,j}$ denotes the threshold of the *j*-th damage diagnosis index for the bridge under diagnosis *v*,

referenced against the bridge p; $U^{p,v,j}$ denotes the damage discrimination index for the j-th wet joint when p serves as the reference bridge and v is the bridge under diagnosis; and U^j denotes the damage discrimination matrix for the j-th wet joint within the clusters.

If the *j*-th wet joint of both the reference bridge p and the bridge under diagnosis v is in an undamaged state, then $U^{p,v,j} = 0$; if at least one of the two bridges sustains damage, then $U^{p,v,j} > 0$. By leveraging this cross-validation strategy, it is possible to diagnose wet joint damage for all the beam bridges monitored within one cluster, thereby avoiding potential misjudgments due to randomness and enhancing the accuracy of the algorithm. The specific procedure for damage diagnosis for wet joints of prefabricated beam bridges monitored within one cluster using the data obtained from distributed optical sensing fibers is illustrated in Fig. 5.

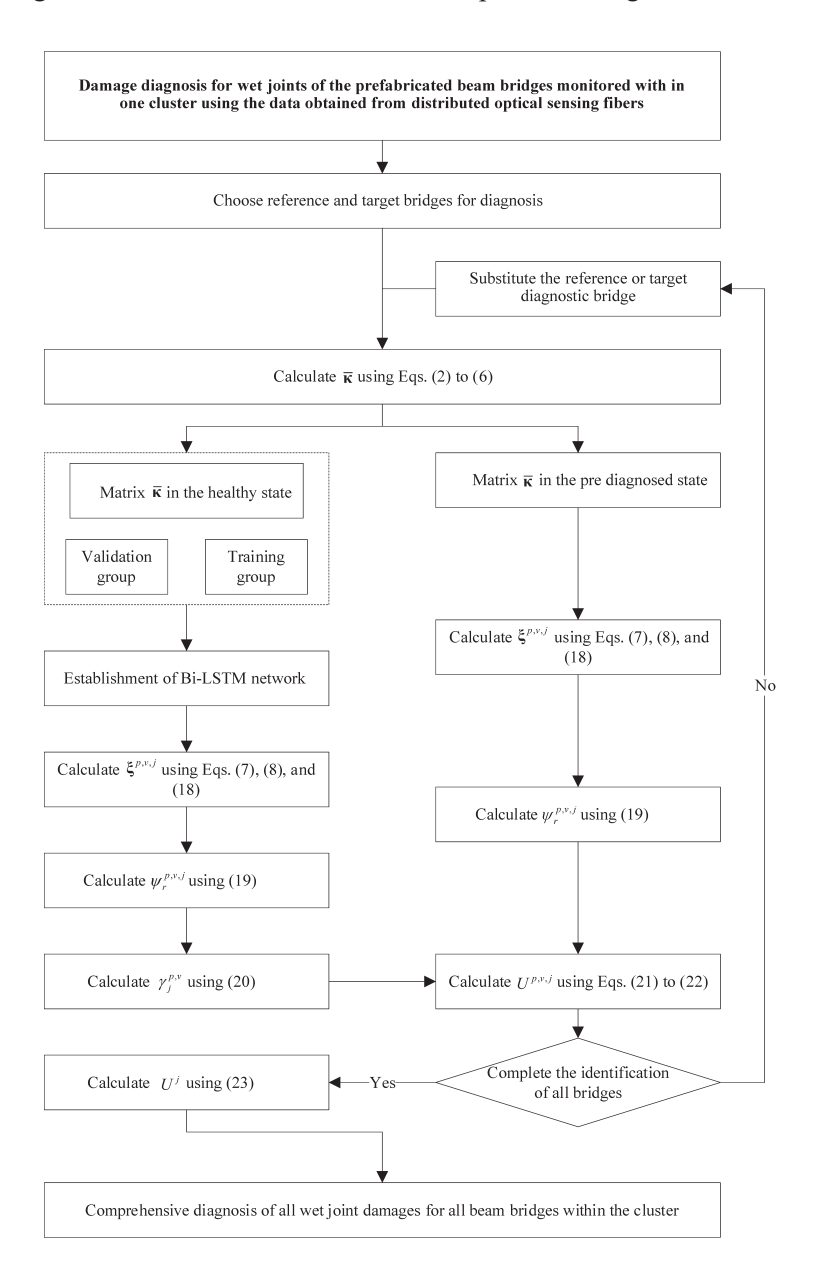


Fig. 5. Flowchart of damage diagnosis for wet joints of the prefabricated beam bridges monitored within one cluster using the data obtained from distributed optical sensing fibers.

3. Case Study Validation

3.1 Brief introduction

An actual prefabricated beam bridge monitored within one cluster was selected to validate the effectiveness of the proposed method. The total length of the line of the prefabricated beam bridge cluster was approximately 44 km, comprising 35113 m/33 bridges, of which the total length of the continuous viaduct of the main line was approximately 15.79 km and the total length of the continuous viaduct of the connecting line was approximately 11.46 km. The prefabricated beam bridges monitored within one cluster are shown in Fig. 6.

In the bridge cluster, three distributed optical-fiber monitoring loops are installed on the top and bottom of the main-girder webs, each measuring 950 m in length. Using a BOTDA analyzer, we acquire curvature data at structural measurement points of the bridge together with the ambient-temperature time history at the bridge site, thereby enabling the real-time monitoring of the structural state of prefabricated beam bridges. The detailed parameters of the BOTDA analyzer are listed in Table 1; the distributed optical-fiber layout for a single bridge within the cluster is shown in Fig. 7, and the fiber deployment process is shown in Fig. 8.



Fig. 6. (Color online) Photograph of the assembly beam bridge cluster.

Table 1 Parameters of the BOTDA analyzer.

Model type	Sensing range	Sampling resolution	Sensing optical fiber	Measurement metrics
RP2050	50 km (loop)	0.2 m	SMF	Temperature, strain
Laser wavelength	Frequency sweeping	Frequency sweeping	Operating	Measuring accuracy
	range	step	temperature	
~1550 nm	10-13 GHz	1–20 MHz	0-40 °C	0.2 °C/4 με

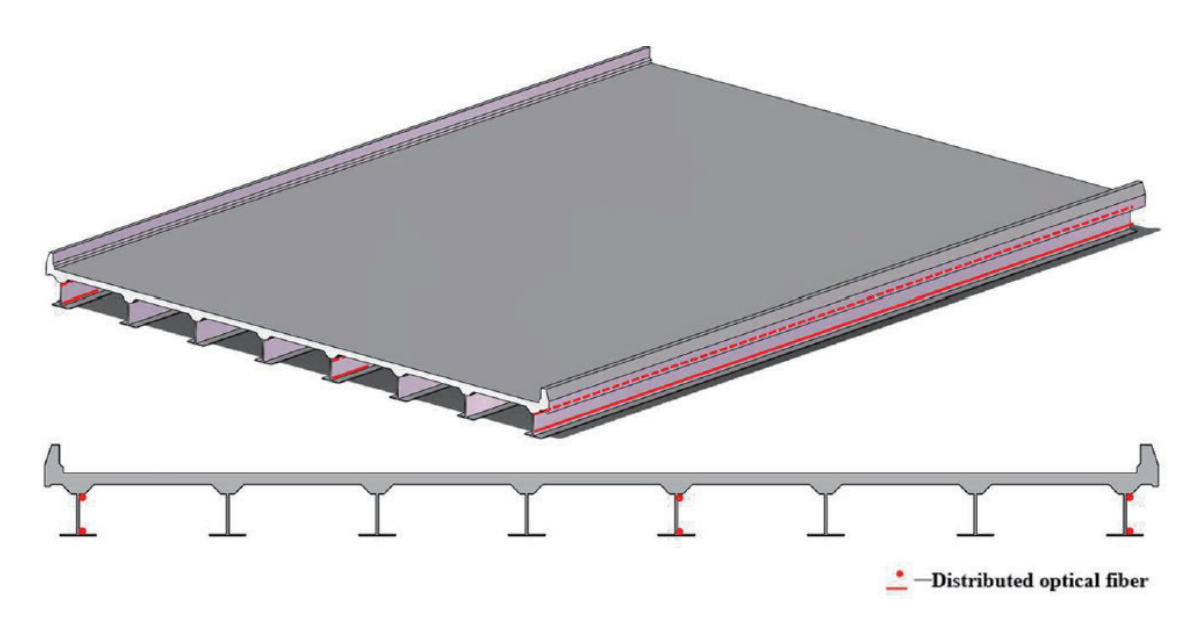


Fig. 7. (Color online) Schematic diagram of the distributed optical sensing fiber layout scheme.



Fig. 8. (Color online) On-site photograph of the distributed optical sensing fiber installation.

3.2 Validation of the performance of the proposed method

Three π -shaped steel–concrete composite simply supported beam bridges with identical structural configurations were selected from the cluster finite element models for these bridges, which were developed using ANSYS finite element software. The three bridges were designated Bridges A, B, and C. All three bridges had identical cross-sectional dimensions, with a span length of 20 m. Both the bridge deck and wet joints were constructed with C50 concrete, and the elastic modulus of the concrete exhibited a linear relationship with the ambient temperature. The steel beams were fabricated from Q255D material. The bridge structures were simulated using SOLID65 solid elements. Connections between the bridge deck and steel beams, as well as between the steel and cross beams, were established via shared nodes. Three monitoring circuits

were placed at the web locations of the model. Key points were defined at critical locations such as the bearings and mid-span, and the mesh between key points was uniformly partitioned with an element size of 10 cm. Three monitoring circuits were placed at the web locations of the model. The cross-sectional dimensions of the bridge are presented in Fig. 9, the linear relationship between the elastic modulus and temperature is illustrated in Fig. 10, and the placement of the monitoring circuits is shown in Fig. 11.

To simulate the random vehicle loading conditions during the operational period, a two-axle vehicle model was employed for loading, and the Monte Carlo method was utilized to acquire arbitrary random vehicle weight information. The probability density function of the vehicle load distribution is presented in Eqs. (24) and (25), while the probability distribution of the random vehicle load is illustrated in Fig. 12.

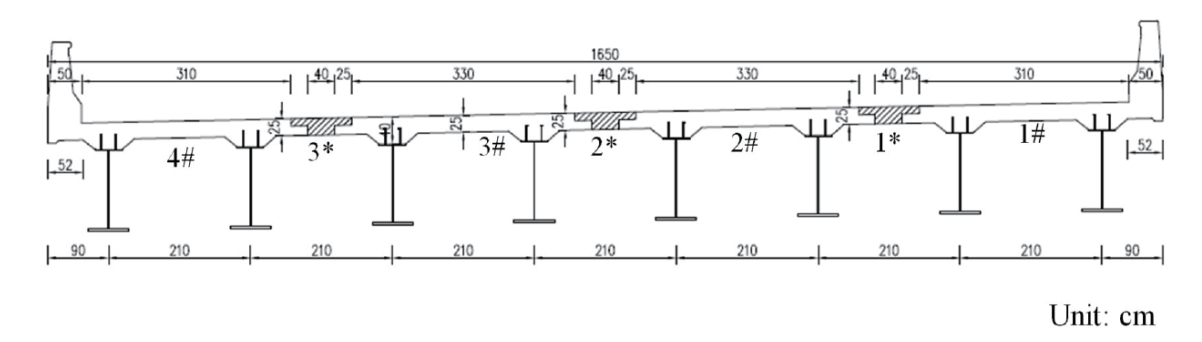


Fig. 9. Schematic diagram of the cross-sectional dimensions of the π -shaped composite.

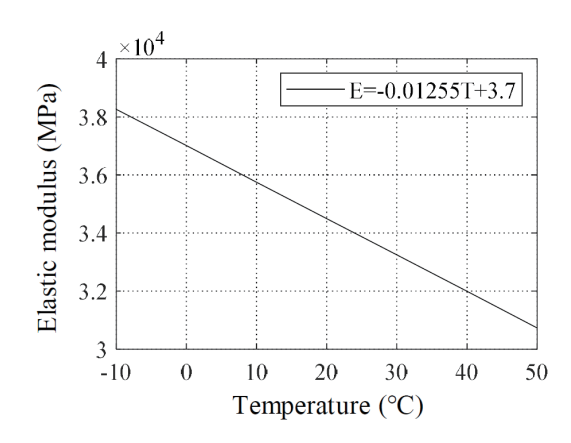


Fig. 10. Relationship between the ambient temperature and the elastic modulus of C50 concrete.

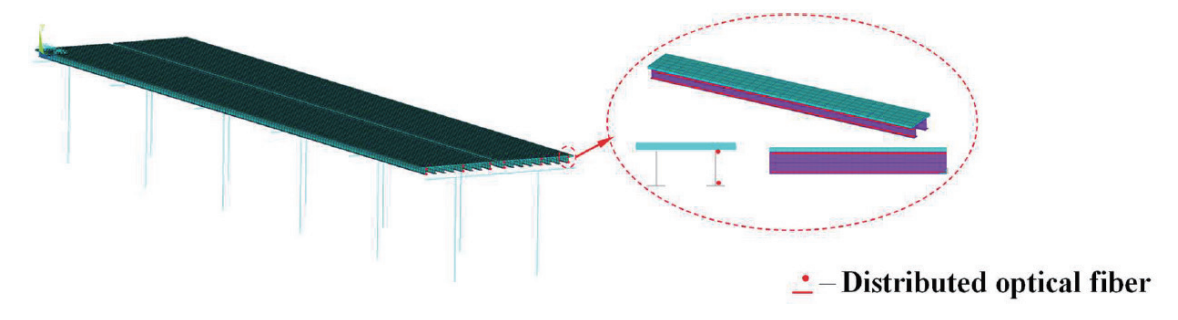


Fig. 11. (Color online) Schematic diagram of the monitoring loop locations.

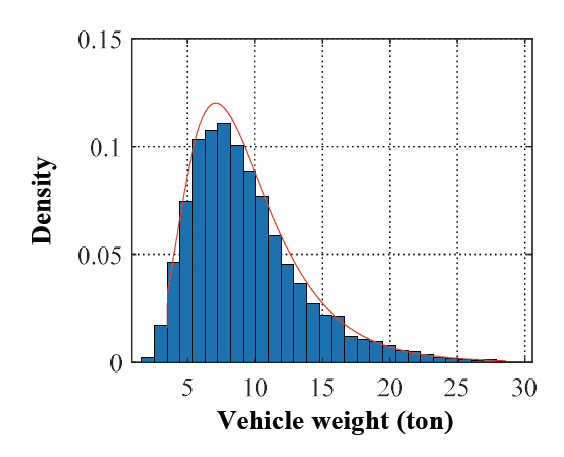


Fig. 12. (Color online) Histogram of simulated vehicle weight frequencies.

$$f(x) = \begin{cases} 0, & x \le b_1 \\ a \cdot \frac{1}{\sqrt{2\pi\sigma}x} e^{-\frac{1}{2}\left(\frac{\ln(x) - \mu}{\sigma}\right)^2}, & b_1 \le x \le b_2 \\ 0, & x > b_2 \end{cases}$$
 (24)

Here, the distribution parameters are $\mu = 2.150068$, $\sigma = 0.4345666$, $b_1 = 3.5$, and $b_2 = 28.62$; the expression for a is

$$a = \frac{1}{\int_{b_1}^{b_2} \frac{1}{\sqrt{2\pi}\sigma x} e^{-\frac{1}{2} \left(\frac{\ln(x) - \mu}{\sigma}\right)^2} dx}.$$
 (25)

The damage process of a wet joint initiates with localized longitudinal cracking at the lower end. As the damage progresses, the damage length propagates in both the vertical and longitudinal directions of the bridge, ultimately reaching a fully damaged state of the wet joint. Accordingly, we define four damage levels for wet-joint elements—healthy, mild damage, moderate damage, and severe damage—by adopting a stiffness reduction (element birth—death) scheme. (24,25) The element deactivation patterns corresponding to the four levels are shown in Fig. 13. In practice, wet joint damage most frequently occurs near the interface between the heavy vehicle lane and the regular traffic lane, i.e., at the wet joint between the edge girder and the neighboring girder. To evaluate the diagnostic performance of the proposed method for wet joint damage, the damage location is set at wet joint 1* on Bridge B. The case configurations for the different damage levels are summarized in Table 2.

To validate the effectiveness of the proposed method, the daily maximum and minimum average temperatures in the region where the bridge is located were simulated over a 28 month period. On the basis of this simulation, a temperature variation—time—history curve was generated, as illustrated in Fig. 14.

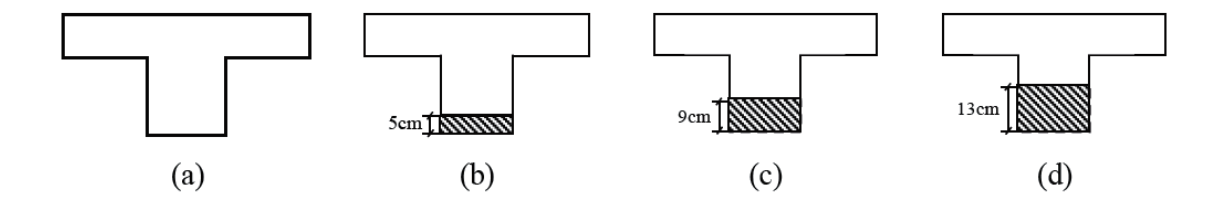


Fig. 13. Schematic diagram of wet joint damage levels. (a) Healthy, (b) mild damage, (c) moderate damage, and (d) severe damage.

Table 2 Bridge wet joint damage conditions.

Damage condition	Damage location	Damage severity	Damage length (cm)	Noise level
Case 1	Bridge B Wet Joint 1*	Mild damage	5	5
Case 2	Bridge B Wet Joint 1*	Moderate damage	9	5
Case 3	Bridge B Wet Joint 1*	Severe damage	13	5
Case 4	Bridge B Wet Joint 1*	Mild damage	5	10
Case 5	Bridge B Wet Joint 1*	Mild damage	5	20

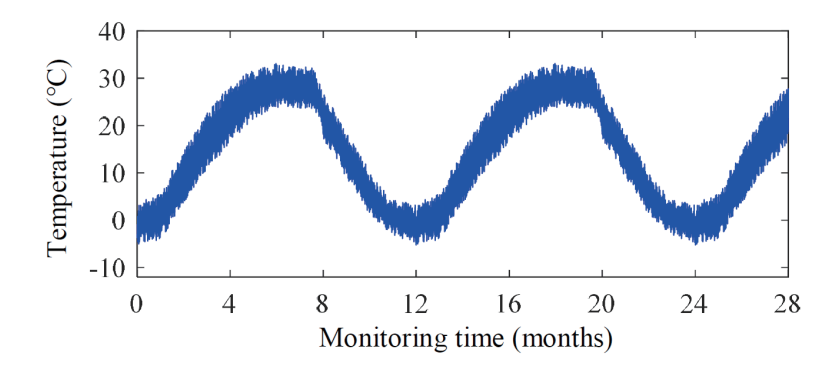


Fig. 14. (Color online) Time history of ambient temperature.

On the basis of the damage conditions specified in Table 1, the strain values at the measurement points and the values of the sectional curvature of the main beam were simulated over a period of 28 months. The first 24 months corresponded to the healthy state, whereas the last 4 months represented the state requiring diagnosis. The sectional curvature of the main beam was subsequently calculated using Eq. (2) and compared with the simulated sectional curvature values of the main beam. Owing to space constraints, only the daily maximum curvature information at the mid-span position of the right-side beam of Bridge B under the healthy state and working conditions 1, 2, and 3 within the 28-month period is presented here. The results are illustrated in Fig. 15.

Among these results, the maximum relative error between the curvature simulation data and the curvature data calculated using Eqs. (2)–(6) is 2.2%. Additionally, a comparison of the simulation results in Figs. 15(b)–15(d) clearly reveals that the changes in curvature data before and after wet joint damage do not intuitively reflect the conditions of wet joint damage.

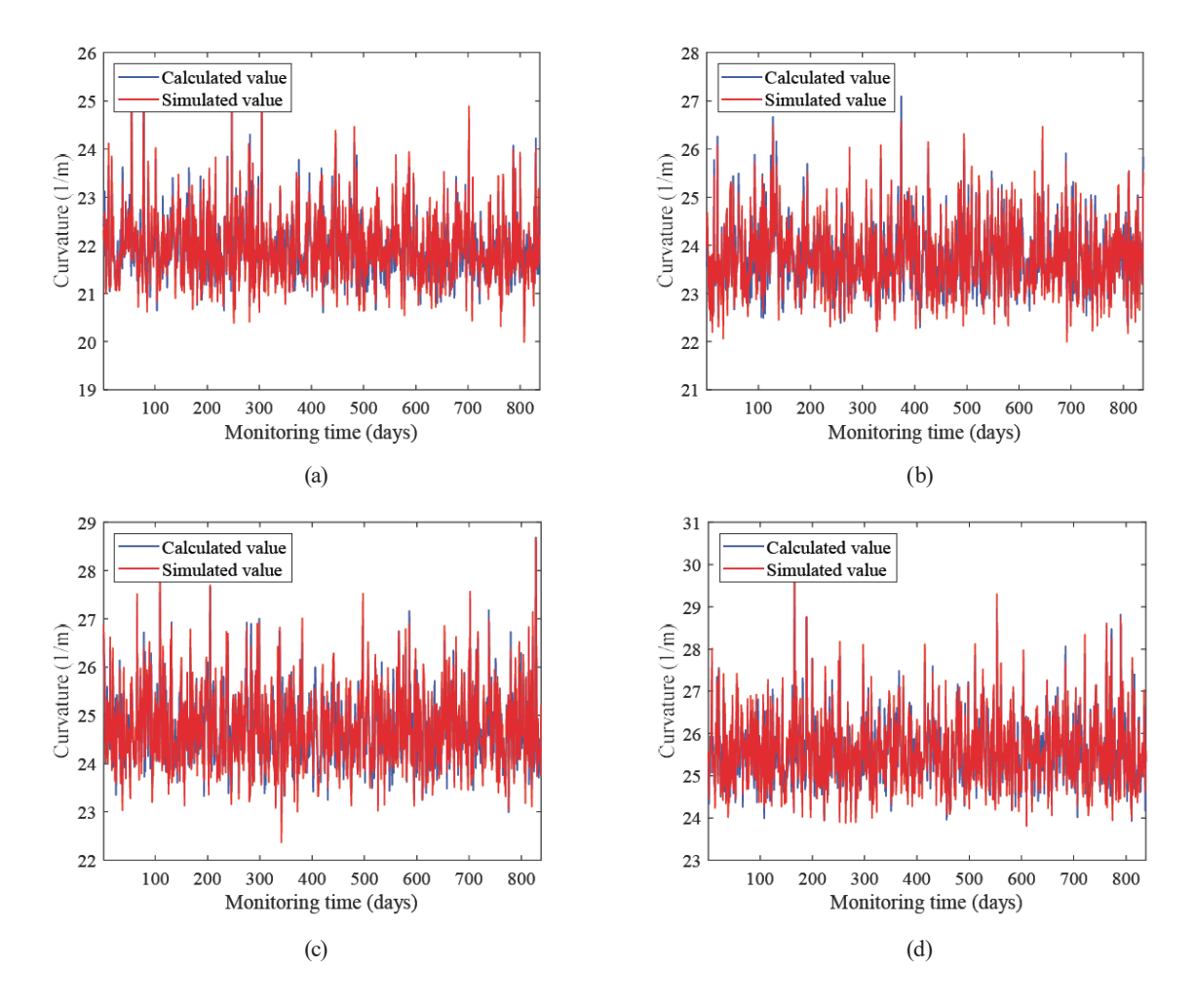


Fig. 15. (Color online) Daily peak curvature at the mid-span location of the right-side beam. Daily peak curvature values of Bridge B in (a) the healthy state, (b) case 1, (c) case 2, and (d) in case 3.

On the basis of the simulation results of the healthy state over the preceding 24 months, Bridges A, B, and C were used as reference and prediction bridges to construct a Bi-LSTM network. In this network, the Adam solver was employed, with the model undergoing 600 iterations, a data time window of 3, and an initial learning rate of 0.005. After 125 epochs, the learning rate was updated using a reduction factor of 0.2. Eighty percent of the data in the curvature matrix were allocated to the training set, whereas 20% were assigned to the validation set to evaluate the predictive effectiveness of the constructed network. On the basis of the simulation results of the diagnostic state over the subsequent four months, the procedure illustrated in Fig. 5 was utilized to determine the wet joint damage state of Bridge B under working conditions 1–5, with the results presented in Figs. 16–20.

From Fig. 16, when Bridge B is subjected to the simulated damage in Case 1, the wet joint damage diagnosis index at wet joint 1* of Bridge B becomes markedly greater than zero when Bridges A and C are used in turn as the reference bridge; conversely, when Bridge B serves as the reference bridge, the indices at wet joints 1* of Bridges A and C are markedly greater than

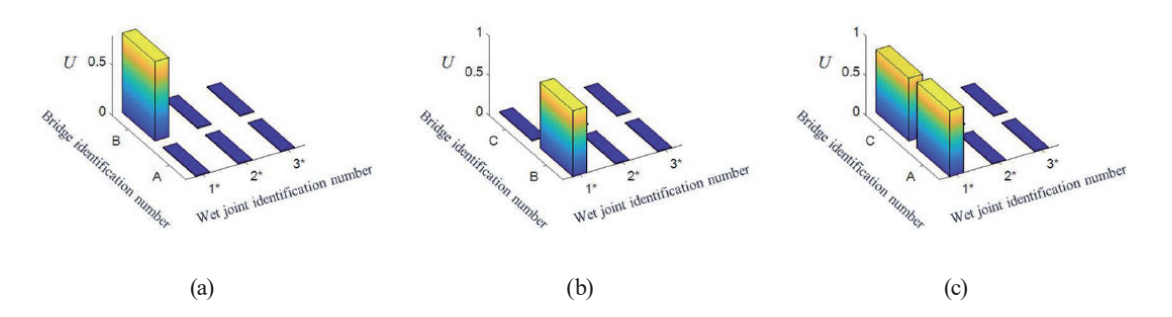


Fig. 16. (Color online) Damage diagnosis results for wet joints in case 1. (a) Bridge C served as the reference bridge, (b) Bridge A served as the reference bridge, and (c) Bridge B served as the reference bridge.

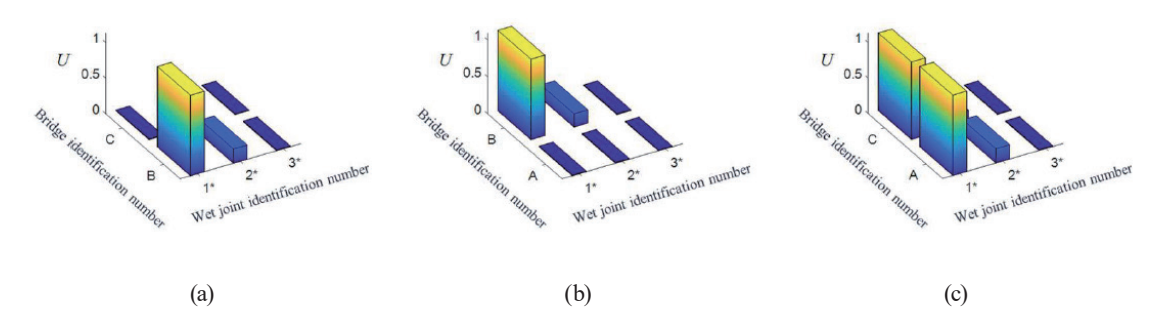


Fig. 17. (Color online) Damage diagnosis results for wet joints in case 2. (a) Bridge C served as the reference bridge, (b) Bridge A served as the reference bridge, and (c) Bridge B served as the reference bridge.

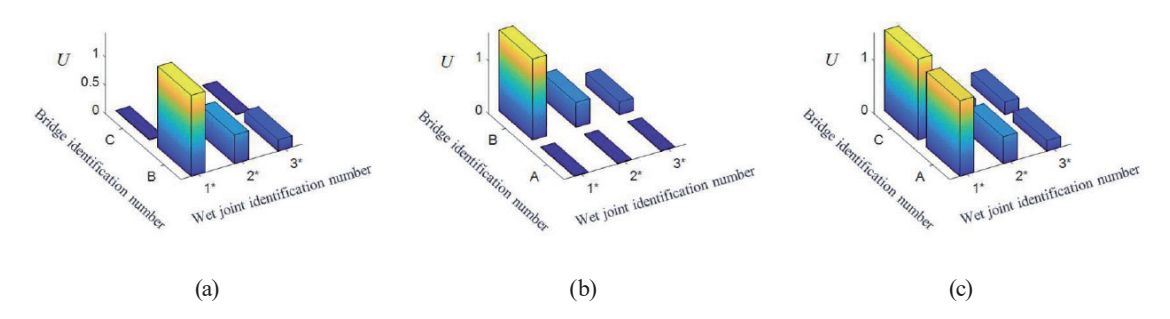


Fig. 18. (Color online) Damage diagnosis results for wet joints in case 3. (a) Bridge C served as the reference bridge, (b) Bridge A served as the reference bridge, and (c) Bridge B served as the reference bridge.

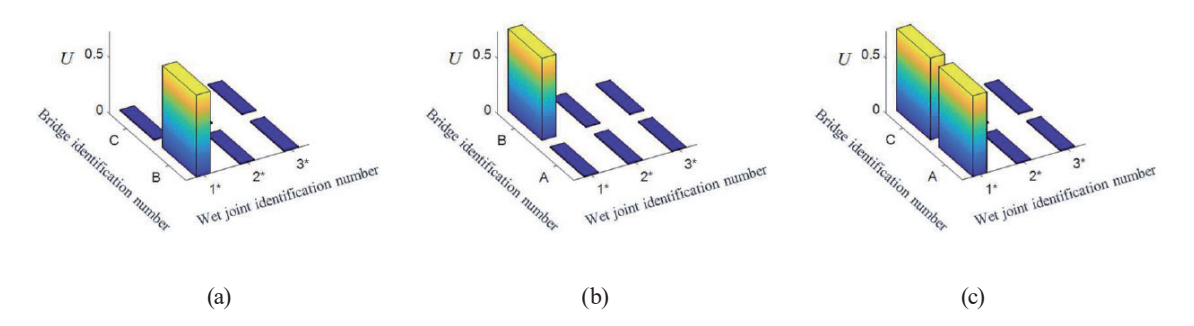


Fig. 19. (Color online) Damage diagnosis results for wet joints in case 4. (a) Bridge C served as the reference bridge, (b) Bridge A served as the reference bridge, and (c) Bridge B served as the reference bridge.

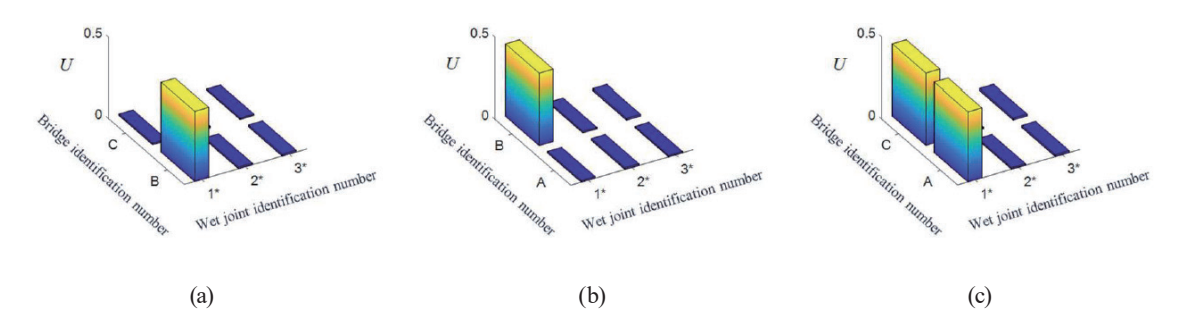


Fig. 20. (Color online) Damage diagnosis results for wet joints in case 5. (a) Bridge C served as the reference bridge, (b) Bridge A served as the reference bridge, and (c) Bridge B served as the reference bridge.

zero. These results indicate a clear discrepancy between the state of wet joint 1* on Bridge B and those on Bridges A and C, suggesting that wet joint 1* of Bridge B is likely damaged. The data in Fig. 16 therefore demonstrate that the proposed wet joint damage diagnosis index effectively reveals differences between the reference bridge and the bridge under diagnosis. However, using a single reference bridge is susceptible to the wet-joint condition of that reference itself and may lead to the misdiagnosis of the bridge under diagnosis; hence, a cross-validation strategy is needed to avoid such errors.

A comparison of the data in Figs. 16–18 reveals that when Bridge B is subjected to the simulated damage in Cases 1–3, the increasing severity at wet joint 1* is accompanied by pronounced deviations from the healthy state at wet joints 2* and 3*. This finding indicates that at the onset of wet joint damage at a specific location, the mechanical performance does not decrease sharply; instead, load redistribution occurs locally near the damage, whereas locations far from the damage remain essentially unaffected. Once the damage exceeds a certain threshold, the mechanical performance degrades significantly, and a global load redistribution emerges across the bridge, causing all wet joints to exhibit abnormal responses.

A comparison of Figs. 16, 19, and 20 clearly reveals that the diagnostic results of the proposed algorithm at a noise level of 10% are largely consistent with those at a noise level of 5%. However, at a noise level of 20%, a reduction in wet joint damage discrimination index was observed, suggesting that noise can affect the diagnostic accuracy of the algorithm to some extent. Nevertheless, the results indicate that the proposed algorithm remains capable of effectively identifying wet joint damage across noise levels ranging from 5 to 20%.

To further validate the diagnostic performance of the proposed method, the damage scenarios listed in Table 1 were analyzed using the lateral deformation influence line method. (26) In this experiment, a standard two-axle vehicle with an axle spacing of 3.8 m, an axle width of 1.8 m, and a total weight of 20 t was employed. After each loading cycle, the vehicle was laterally shifted by 0.55 m, and the process was repeated for a total of 30 cycles. Displacement measurement points were established at the bottom of the quarter-span, mid-span, and three-quarter-span positions along the centerline of each girder. A schematic diagram of the load test is shown in Fig. 21, and the diagnostic outcomes are depicted in Fig. 22.

As shown in Fig. 22, the diagnostic index of the transverse deformation influence line method was approximately zero under mild wet joint damage conditions, indicating its limited

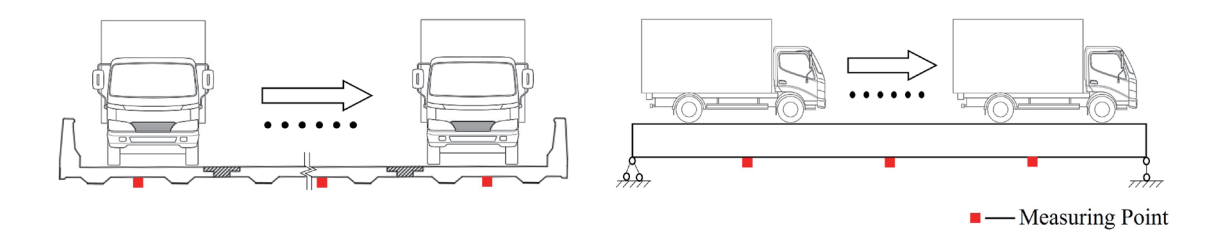


Fig. 21. (Color online) Schematic diagram of test vehicle loading.

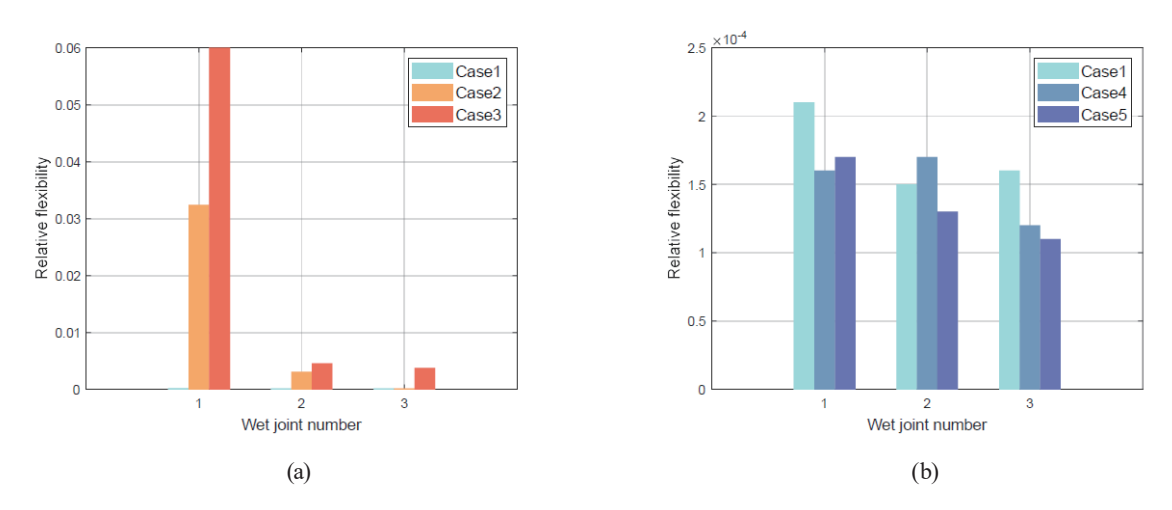


Fig. 22. (Color online) Schematic diagram of wet joint damage diagnosis results. (a) Diagnostic results for cases 1, 2, and 3. (b) Diagnostic results for cases 1, 4, and 5.

effectiveness in diagnosing early-stage wet joint damage. As shown in Fig. 22(a), as the damage to the 1* wet joint increased, both the 2* and 3* wet joints exhibited damaged states, and the bridge experienced load redistribution. These observations align with the conclusions drawn from Figs. 16 to 18, thereby validating the effectiveness of the proposed method in this study.

3.3 Data analysis of real bridge monitoring

In addition, strain monitoring data were collected for the fifth, sixth, and seventh span bridges within the prefabricated beam bridges monitored within one cluster during the initial four months after construction and one month of operation. The wet joint conditions of these three bridges were subsequently evaluated. Owing to space constraints, in this paper, we present only the daily maximum curvature calculation results at the 1/4 span, mid-span, and 3/4 span positions of the side beam of the fifth span bridge, as well as the wet joint damage diagnosis results for all three bridges. An actual bridge is shown in Fig. 23, the daily maximum curvature calculation results are shown in Fig. 24, and the diagnosis results are shown in Fig. 25.

As shown in Fig. 24, when each of the three bridges was used as both the reference bridge and the target bridge for diagnosis, the wet joint damage discrimination index remained consistently below 0.07 and approached zero. These findings demonstrate that while the



Fig. 23. (Color online) Photograph of an actual bridge.

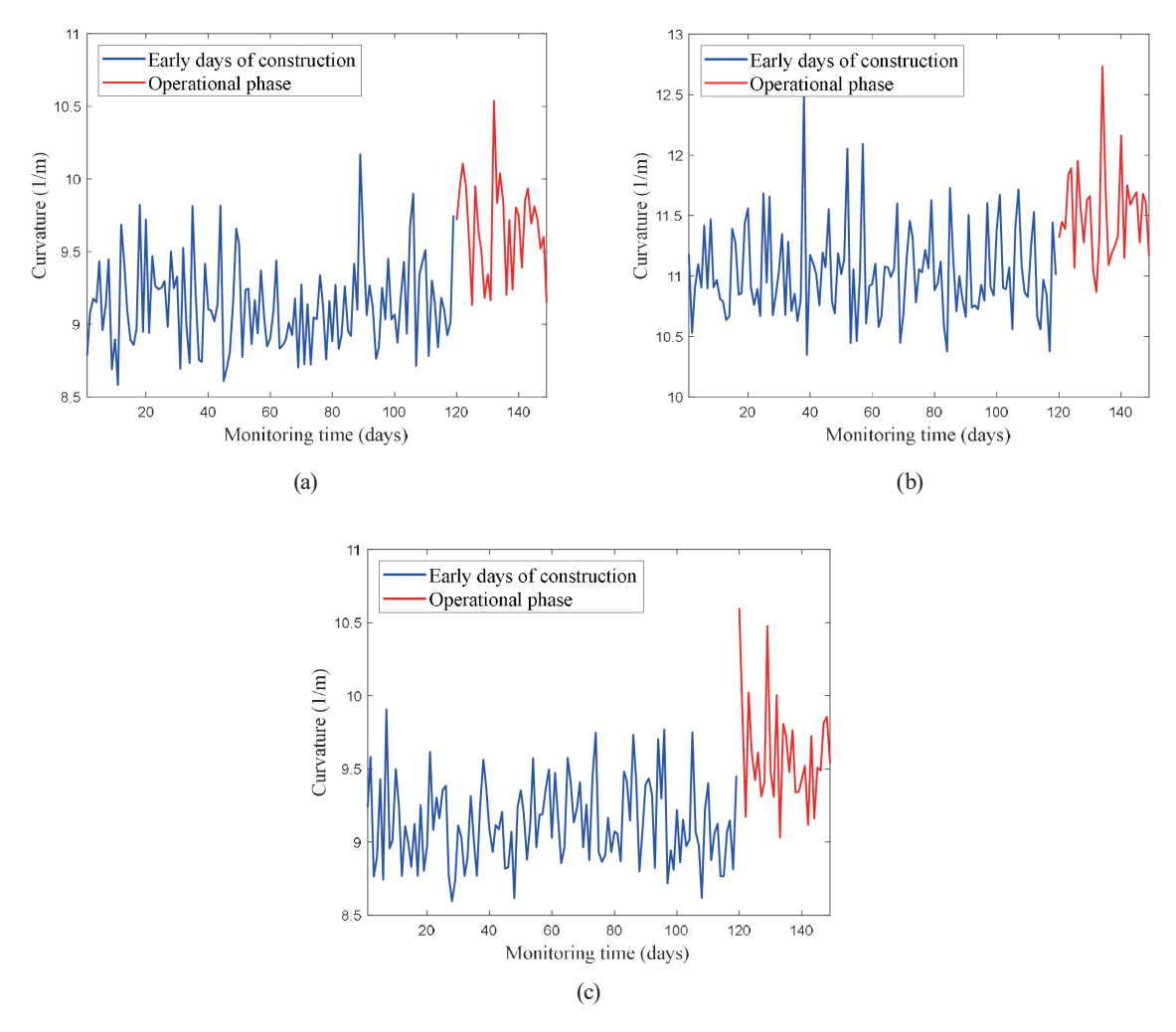


Fig. 24. (Color online) Results of daily maximum curvature calculations. Maximum daily curvature values measured at the (a) one-quarter span, (b) mid-span, and (c) three-quarter span positions.

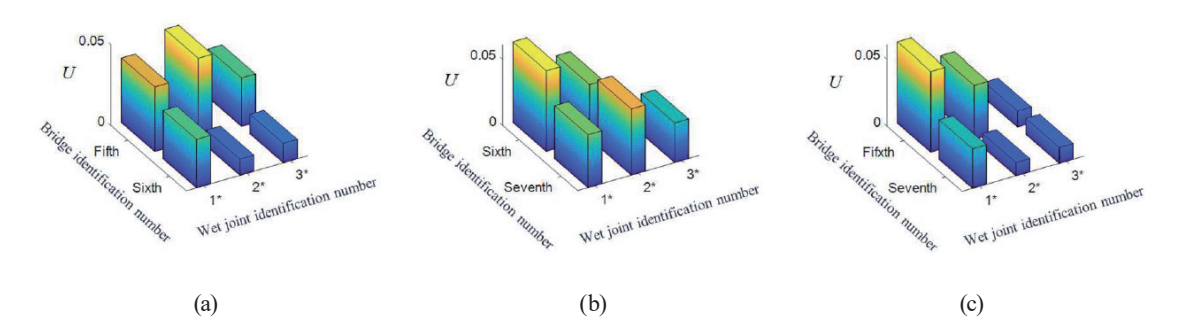


Fig. 25. (Color online) Wet joint damage diagnosis results. (a) The seventh link bridge served as the reference bridge, (b) the fifth link bridge served as the reference bridge, and (c) the sixth link bridge served as the reference bridge.

proposed algorithm cannot fully eliminate the effects of environmental noise and other factors on the diagnostic results, such effects are negligible and will not result in the misjudgment of the wet joint condition.

4. Conclusions

To achieve an effective diagnosis of wet joint damage in prefabricated beam bridges monitored within one cluster, we proposed a diagnostic method for wet joint damage in such clusters on the basis of data obtained from distributed optical sensing fibers. The main conclusions are as follows:

- The proposed algorithm uses the spatiotemporal correlation of prefabricated beam bridges monitored within one cluster to construct a Bi-LSTM network, enabling the mutual prediction of the sectional curvature of the main beam among identical bridges within the cluster. On this basis, a discriminant index for wet joint damage is developed, allowing for the effective diagnosis of wet joint damage within such clusters.
- 2. The results of the numerical examples indicate that in the early stage of wet joint damage in prefabricated beam bridges, load redistribution occurs only near the damaged location, whereas the load distribution at healthy locations remains largely unchanged. As the damage at the wet joint location worsens, the overall load-bearing capacity of the bridge decreases, and the wet joints at healthy locations begin to experience abnormal stress conditions.
- 3. The proposed algorithm is specifically designed for monitoring wet joint damage in identical prefabricated beam bridges monitored within one cluster. Additionally, since the algorithm employs a cross-validation strategy, it is applicable only when there are more than three identical prefabricated beam bridges in the cluster.
- 4. The analysis of the monitoring data from the actual bridge reveals that, while the proposed method cannot fully eliminate the effects of environmental noise and other factors on the diagnostic outcomes, these effects are negligible and will not result in the misjudgment of the wet joint condition.

Acknowledgments

This work was supported by the Engineering Construction Research Project of Zhejiang Provincial Department of Transportation (No. 2022-GCKY-03).

References

- 1 Statistical Bulletin on the Development of the Transportation Industry in 2024. https://xxgk.mot.gov.cn
- 2 W. Wu, H. Zhang, Z. Liu, and Y. Wang: Mater. 15 (2022) 6805. https://doi.org/10.3390/ma15196805
- 3 Y. Liu and M. Gao: Comput.-Aided Civ. Infrastruct. Eng. 37 (2022) 1891. https://doi.org/10.1111/mice.12874
- 4 D. Ji, C. Li, C. Zhai, and Z. Cao: IEEE Trans. Geosci. Remote Sens. 62 (2024) 1. https://doi.org/10.1109/TGRS.2024.3409620
- 5 Q. Xia, Y. Zhou, Y. Cheng, and J. Zhang: Struct. Control Health Monit. 2023 (2023) 1. https://doi.org/10.1155/2023/1834669
- 6 D. Yang, H. Zhou, T. Yi, H. Li, and H. Bai: Struct. Control Health Monit. 29 (2022) 3053. <u>https://doi.org/10.1002/stc.3053</u>
- 7 S. Li, H. Yang, P. Guo, D. Ren, B. Xu, and Z. Liang: Measurement. **224** (2024) 113867. https://doi.org/10.1016/j.measurement.2023.113867
- 8 Z. Shang, F. Gong, Z. Shao, J. Matos, G. Xin, and Y. Xia: Sensors 24 (2024) 4255. https://doi.org/10.3390/s24134255
- 9 F. Han, D. Dan, Z. Xu, and Z. Deng: Struct. Control Health Monit. 21 (2022) 2010. https://doi.org/10.1177/14759217211047899
- 10 D. Dan, W. Zheng, and Z. Xu: Structures 48 (2023) 1322. https://doi.org/10.1016/j.istruc.2023.01.023
- H. Hu, J. Wang, C.-Z. Dong, J. Chen, and T. Wang: Mech. Syst. Signal Process. 183 (2023) 109631. https://doi.org/10.1016/j.ymssp.2022.109631
- 12 F. Gong, X. Lei, and Y. Xia: Eng. Struct. 300 (2024) 117147. https://doi.org/10.1016/j.engstruct.2023.117147
- 13 J. Zhan, F. Zhang, M. Siahkouhi, X. Kong, and H. Xia: Eng. Struct. **228** (2021) 111551. https://doi.org/10.1016/j.engstruct.2020.111551
- 14 M. Abedin, F. J. De Caso y Basalo, N. Kiani, A. B. Mehrabi, and A. Nanni: Eng. Struct. **252** (2022) 113648. https://doi.org/10.1016/j.engstruct.2021.113648
- 15 F. Han, D. Dan, Z. Xu, and Z. Deng: Struct. Health Monit. 21 (2022) 2010. https://doi.org/10.1177/14759217211047899
- 16 A. J. Reiff, M. Sanayei, and R. M. Vogel: Eng. Struct. **109** (2016) 139. https://doi.org/10.1016/j.engstruct.2015.11.006
- 17 Z. Zhou, K. Dong, Z. Fang, and Y. Liu: Sustainability 14 (2022) 10019. https://doi.org/10.3390/su141610019
- 18 Z. Zhou, Y. Liu, and H. Dai: Measurement 208 (2023) 112448. https://doi.org/10.1016/j.measurement.2023.112448
- 19 Z. Zhou, Y. Liu, and H. Li: Measurement 211 (2023) 112611. https://doi.org/10.1016/j.measurement.2023.112611
- 20 Q. Xu, Z. Zhou, and Y. Liu: Struct. Control Health Monit. 2023 (2023) 1. https://doi.org/10.1155/2023/8234927
- 21 Z. Zhou, X. Ma, Y. Liu, and H. Li: Struct. Health Monit. 24 (2025) 351. https://doi.org/10.1177/14759217241236368
- 22 Z. Zhou, Q. Xu, Q. Gao, and Y. Liu: Eng. Syst. Part B: Mech. Eng. 10 (2024) 4065268. https://doi.org/10.1115/1.4065268
- 23 M. Zhao, X. Yi, J. Zhang, and C. Lin: Front. Earth Sci. (Lausanne). 9 (2021) 660918. https://doi.org/10.3389/feart.2021.660918
- 24 C. S. N. Pathirage, J. Li, L. Li, H. Hao. W. Liu, P. Ni: Eng. Struct. 172 (2018) 13. https://doi.org/10.1016/j.engstruct.2018.05.109
- 25 F. I. Sakiyama, G. S. Veríssimo, F. Lehmann, H. Garrecht: Struct. Health Monit. 22 (2023) 496. https://doi.org/10.1177/14759217221079295
- 26 D. Yang, H. Zhou, T. Yi, H. Li, and H. Bai: Struct. Control Health Monit. 29 (2022) 3053. https://doi.org/10.1002/stc.3053